Characterizing plasma conditions in radiatively heated solid-density samples with x-ray Thomson scattering

A. M. Saunders, B. Lahmann, G. Sutcliffe, J. A. Frenje, R. W. Falcone, and T. Döppner

Phys. Rev. E **98**, 063206 — Published 26 December 2018

DOI: 10.1103/PhysRevE.98.063206

Characterizing Plasma Conditions in Radiatively-Heated Solid Density Samples with X-Ray Thomson Scattering

A. M. Saunders,[1,2,*] B. Lahmann,[3] G. Sutcliffe,[3] J. A. Frenje,[3] R. W. Falcone,[1] and T. Döppner[2]

[1] *Physics Department, University of California Berkeley, Berkeley, California 94709, USA*
[2] *Lawrence Livermore National Laboratory, Livermore, California 94550, USA*
[3] *Plasma Science and Fusion Center, Massachusetts Institute of Technology, Cambridge, Massachusetts 02139, USA*

(Dated: November 18, 2018)

We have developed an experimental platform to generate radiatively heated solid density samples for warm dense matter studies at the OMEGA laser facility. Cylindrical samples of boron and beryllium are isochorically-heated by K- and L-shell emission from x-ray converter foils wrapped around the cylinders' radii. X-ray Thomson scattering (XRTS) measures the temperature and the ionization state of the samples as function of time. Temperatures approach 10 eV, and the ionization states are found to be $Z_B = 3$ and $Z_{Be} = 2$. Radiation hydrodynamics simulations were performed to confirm a homogeneous plasma state exists in the center of the sample for the duration of the experiment. Results from the study can be extended to improve understanding of radiative heating processes in the warm dense matter regime.

I. INTRODUCTION

Warm dense matter (WDM) is an area of active theoretical and experimental investigation due to its relevance to planetary interiors [1], brown dwarfs [2], and inertial confinement fusion research [3–11]. WDM is nominally defined as matter with a coupling parameter of $\Gamma \sim 1$, i.e. the Coulomb energy is on the same order as the thermal energy [12]. This regime corresponds with near solid densities and temperatures on order of the Fermi temperature, and typically consists of partially ionized atoms. This range of densities, temperatures, and ionization states presents significant challenges to theory and modeling, as quantum and coupling effects cannot be treated as perturbations and the standard simplifying approximations that are often made in plasma or condensed matter physics cannot be applied.

The heating of matter by x-ray radiation plays an important role in a range of WDM experiments, as well as in high energy density research [13–15], experiments that pursue inertial confinement fusion [16], and astrophysical processes [17–19]. For example, x-ray heating is used to generate uniform and controlled WDM conditions for ion stopping power measurements on beryllium, as seen in recent experiments [20] on the OMEGA Laser [21]. These experiments relied on simulations of plasma conditions to interpret the experimental results; electron density, electron temperature, and fractional ionization all affect how charged particles deposit their energy and are particularly challenging to model in the WDM regime [20, 22]. Having a means of measuring these conditions could greatly improve the inferences made from ion stopping power experiments in WDM plasmas.

X-ray Thomson scattering (XRTS) has emerged as an experimental technique to probe the complicated physics of WDM [4, 23–27] as it offers the ability to measure plasma conditions such as electron density, electron temperature, and ionization state [28]. In an XRTS measurement, a narrow-bandwidth x-ray source impinges on a plasma and scatters into a spectrometer at a desired scattering angle. The spectrum of inelastically scattered x-rays reflects the electron velocity distribution and thus the electron temperature, electron density, or both, as x-rays scatter inelastically from free and loosely-bound electrons. The elastic component of the scattering spectrum arises from x-rays that scatter from tightly-bound electrons. The ratio of the areas under the elastic and inelastic components reflects the ratio of free or bound electrons and thus the ionization state [28].

Because XRTS directly measures the plasma conditions, it offers an ideal tool to examine modeling uncertainties of x-ray heating in the WDM regime. Here, XRTS is particularly powerful because the mass density is known *a priori* and the XRTS spectra can be used to deduce electron temperature and ionization state. In fact, several experiments on the OMEGA laser have demonstrated the use of XRTS in radiatively heated material [23, 29]. These experiments returned the time dynamics as well benchmarking data for ionization models in high energy density plasmas. However, direct measurements of the conditions in radiatively heated plasmas are sparse and more experiments are needed to constrain predictive models.

In addition, the interpretation of XRTS spectra from the non-uniform, inhomogeneous plasmas formed in complex experimental geometries relies on accurate modeling of how x- rays scatter from plasma electrons [30, 31]. This includes modeling of atomic form factors, structure factors [32, 33], screening contributions [34], and the physics of the electrons that undergo Raman-like transitions to the continuum [4]. There has been limited experimental data available from uniform conditions to validate the many models used in interpreting XRTS data. Indeed, recent XRTS work has come under criticism due to the inconsistent models used in conjunction for the in-

* saunders15@llnl.gov

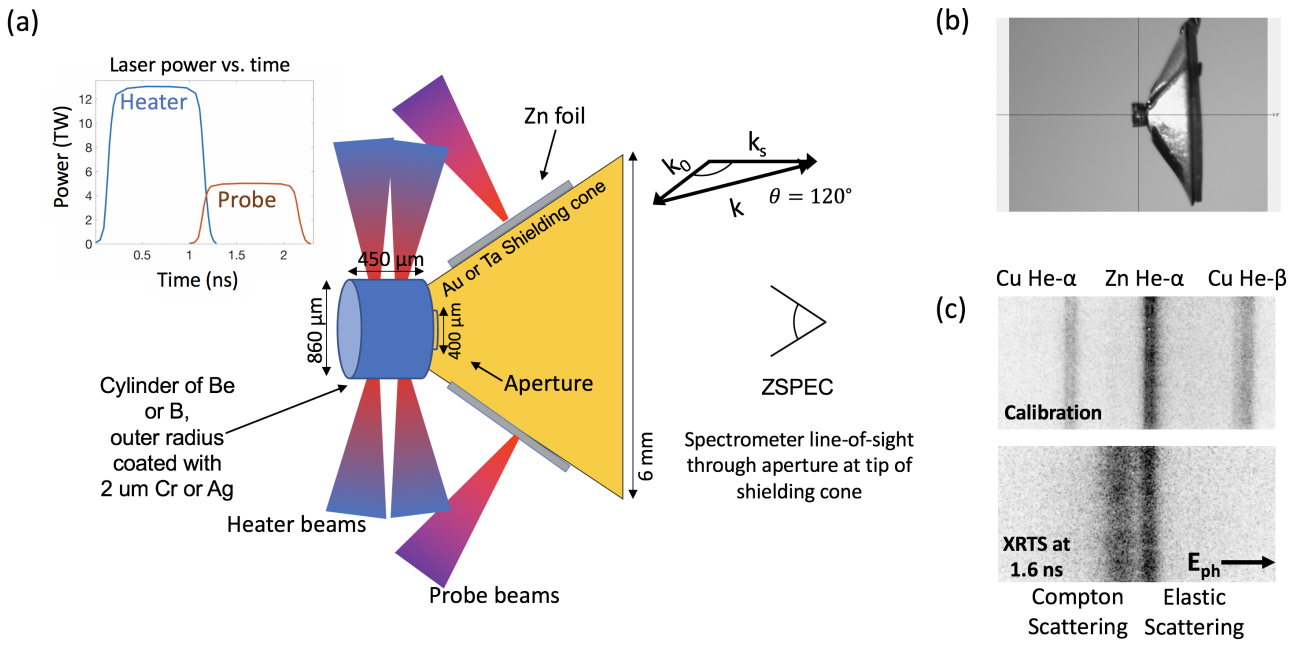

FIG. 1. (a) A schematic of the target geometry, laser configurations, and scattering k-vectors. (b) A photograph of the boron target. (c) Two images of raw data. The top image shows the spectrometer calibration spectrum from a brass foil with the Zn He-α doublet at 8.97 keV in the center of the strip, as well as Cu He-α at 8.37 keV and Cu He-β at 9.87 keV. The bottom picture shows XRTS data from a B sample on the same energy scale as the calibration shot. The elastic scattering feature appears on the right side and the Compton (inelastic) scattering feature is on the left. In both spectra, the photon energy increases from left to right.

elastic and elastic scattering features to interpret plasma properties [35]. Radiatively heated solids provide an opportunity to utilize a known mass density and heating rate to create relatively uniform conditions in order to benchmark modeling of XRTS spectra.

In the following sections, we present XRTS measurements from isochorically heated boron (B) and beryllium (Be) on the OMEGA Laser. The boron and beryllium samples are radiatively heated by x-rays generated from the laser-heated x-ray converter foils of Cr and Ag, respectively. We analyze the results to obtain electron temperature and ionization state as a function of time, and compare the predicted results with radiation hydrodynamics simulations of radiative heating. The results from this platform show the power of XRTS to measure time-resolved plasma conditions in radiatively heated WDM. Finally, we offer a path forward of how to improve the measurements and reach more extreme conditions in the samples.

II. OVERVIEW OF EXPERIMENTAL SETUP AND RESULTS

We begin by presenting an overview of the experiment used to collect XRTS data from radiatively heated warm dense matter.

Figure 1(a) shows a schematic of the target geometry, along with the laser configurations and scattering k-vectors. The cylindrical sample is a (500 ± 100) μm long cylinder with an 860 μm diameter. A (2 ± 1) μm thick x-ray converter foil coats the outer radius of the cylinder. A high-Z material shielding cone with an opening angle of 120° abuts one end of the cylinder and serves to block the spectrometer's direct line-of-sight to the Zn backlighter foils that are glued to the sides of the cone. The cone contains a 400 μm diameter aperture at its tip to allow x-rays scattered by the sample through to the spectrometer, as seen in Figure 1. In the first experimental iteration, the shielding cone was made of 75 μm-thick Au, coated with 10 μm of CH plastic in order to prevent the Au from becoming heated by hot electrons or direct laser irradiation. The appearance of Au line emission around the scattering spectrum prompted the use of a different scattering cone design for subsequent experiments, which used a 3-D printed plastic cone encased with 70 μm-thick Ta foils.

24-26 laser beams heat the x-ray converter foil wrapped around the sample, each providing 500 J at 351 nm in a 1 ns square pulse, as seen in the upper left-hand corner of Figure 1 (indicated as 'heater' beams). The beams were set to best focus without phase plates and were arranged evenly over the surface of the cylinder. Chromium is used as the converter foil material for the boron samples and converts the laser energy to chromium K-shell line emission, which ranges between 5.4-5.9 keV in energy. Silver

is used to heat the beryllium sample and heats the samples through silver L-shell emission, ranging from 3.6-4.2 keV. 6-10 laser beams heat the Zn foils, beginning at 1.2 ns, around the time the inner-cylinder is expected to reach its maximum temperature (indicated as 'probe' beams in the upper left of Figure 1). The 9 keV Zn He-α x-rays that scatter from the sample are collected by the spectrometer, ZSPEC. ZSPEC is a Bragg crystal spectrometer that consists of a 50 mm x 25 mm highly oriented pyrolytic graphite (HOPG) crystal placed equidistantly from a four-strip microchannel plate (MCP). Each strip is time gated and integrates over 180 ps. The axis of the sample cylinder is aligned with the ZSPEC's line-of-sight. The 400 μm aperture in the shielding cone restricts the view of the ZSPEC to the central 500 μm diameter of the cylindrical sample.

The cylinder consists either of solid density beryllium or solid density boron. In both cases, the sample's mass density and purity was characterized by the manufacturer, Goodfellow. The beryllium was characterized to be more than 99.0% pure, with a density of 1.858 g cm^{-3}. The impurities that appear in the highest concentrations are oxygen (at 0.4 atomic percent) due to oxidation of the outer layers, iron (0.07 at.%), and carbon (0.07 at.%); these impurity concentrations are not predicted to affect scattering signals [36]. The boron plugs were also characterized to be more than 99% pure, with a mass density of 2.36 g cm^{-3}.

We collected several time-resolved XRTS spectra from the boron cylinders. The first spectra were taken at 1.5 ns, which was after x-ray backgrounds generated by the interaction of the heater beams with the converter foil began to abate. The latest measurements were taken until 2.0 ns, which was before the shock was expected to come into view of the spectrometer through the aperture in the shielding cone. Data from the beryllium cylinders was limited to a single scattering spectrum at 1.6 ns due to Au x-ray backgrounds from the shielding cone.

III. RADIATION HYDRODYNAMICS SIMULATIONS

We performed 1-D radiation hydrodynamics simulations using the simulation code Helios [37] in order to verify that XRTS measurements were made before the shock front reached the region of the cylinder visible to the spectrometer, i.e. under isochoric conditions, and to obtain predictions for the effects of radiative heating on the samples. The simulations assume a 1 ns square pulse laser drive based on the measured shape of the OMEGA laser and use an average intensity based on number of lasers incident on the surface. We choose to show simulations performed on boron in this section, but the simulations for beryllium are qualitatively similar.

Figure 2 shows the simulated mass density profiles of the boron cylinder versus time. The heater laser drive was measured to be 13 TW at its peak, which correlates

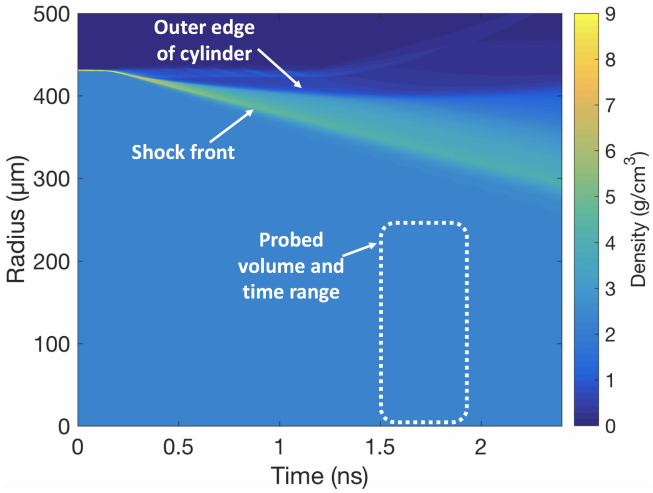

FIG. 2. A plot of 1-D hydrodynamics simulations of boron mass density versus radius and time. The white box indicates the implosion times and region of the cylinder probed by our XRTS measurements. The simulations indicate that XRTS measurements are made before the shock front reaches the region of the cylinder that is probed by x-rays.

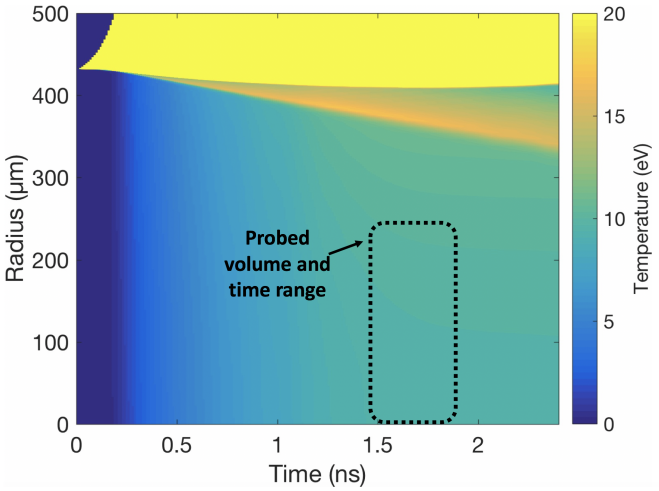

FIG. 3. 1-D radiation hydrodynamics simulations of boron electron temperature versus radius and time. The dashed black box indicates the probed volume and time range measured by XRTS. The simulations show that we expect temperatures to remain relatively constant after the laser drive turns off.

with a laser intensity of $I_0 = 1070$ TW cm^{-2} on the cylindrical surface [1]. The region that is visible by the spectrometer through the aperture in the shielding cone is indicated by the dashed white box, as well as the times that XRTS spectra were measured. The outer edge of

[1] The simulation code Helios requires a laser intensity in the units of TW cm^{-1}, which translates as the areal intensity multiplied by the diameter of the cylinder

the cylinder and the shock front are labeled. As Figure 2 shows, the shock wave does not reach the region that is visible by the spectrometer until after 2.5 ns, increasing certainty in the fact that these measurements were made under isochoric conditions.

We then tuned the output of the simulations to match the temperatures that were measured by XRTS, as will be discussed in Section V, by changing the strength of the laser drive. The simulations reproduced the measured temperatures when the laser drive power decreased to $0.31I_0 = 330$ TW cm^{-2}. Figure 3 shows the simulated electron temperature versus radius and time for the case of the lower laser drive. The simulations predict that the temperature of the sample is expected to stay relatively constant at ~ 9 eV within the times and volume probed by XRTS.

We now describe the methods used to analyze the spectra before showing the results of the analysis.

IV. XRTS THEORY AND PREVIOUS WORK

To perform a full analysis of the collected spectra, we present theory relevant to x-rays scattering from plasma electrons.

In an XRTS experiment, x-rays scatter into the full solid angle as a result of interactions with electrons in the plasma. The scattered power per frequency and per solid angle can be written as [28]:

$$\frac{d^2P}{d\Omega d\omega} = r_0^2 \frac{1}{2}\left(1+\cos^2\theta\right)\left(\frac{\omega_s}{\omega_i}\right)^2 N I_0 S(k,\omega) \quad (1)$$

where P is the scattered power, r_0 is the classical electron radius, θ is the scattering angle, N is the number of scatterers, and I_0 is the intensity incident on the target. The term including $\cos^2\theta$ describes polarization dependence of unpolarized light. $\hbar\omega = \hbar(\omega_i - \omega_s)$ is the change in the photon's energy where ω_i and ω_s are the frequencies of the incident and the scattered photons, respectively. k denotes the magnitude of the wave vector momentum transfer during the scattering and is determined by the scattering angle and incident frequency, by $k = \frac{2}{c}\omega_i \sin\theta/2$.

The oft-applied Chihara decomposition [38, 39] describes the total dynamic structure factor, $S(k,\omega)$, as:

$$S(k,\omega) = |f(k)+q(k)|^2 S_{ii}(k,\omega) \; + \; Z_f S_{ee}(k,\omega) + Z_b \int S_{be}(k,\omega-\omega')S_s(k,\omega')d\omega', \quad (2)$$

where $\hbar\omega$ is the energy transferred from the electron by Compton scattering, $f(k)$ is the ionic form factor, $q(k)$ is the electronic screening cloud contribution, S_{ii} is the ion density correlation function, Z_f is the ionization state, S_{ee} is the free-free dynamic structure factor, Z_b is the bound charge per atom, S_{be} is the form factor of bound electrons undergoing Raman-like transitions to the continuum, which is modulated by the self-motion of the ions, S_s. The three terms represent the contributions from bound-bound, free-free, and bound-free scattering, respectively [38, 39].

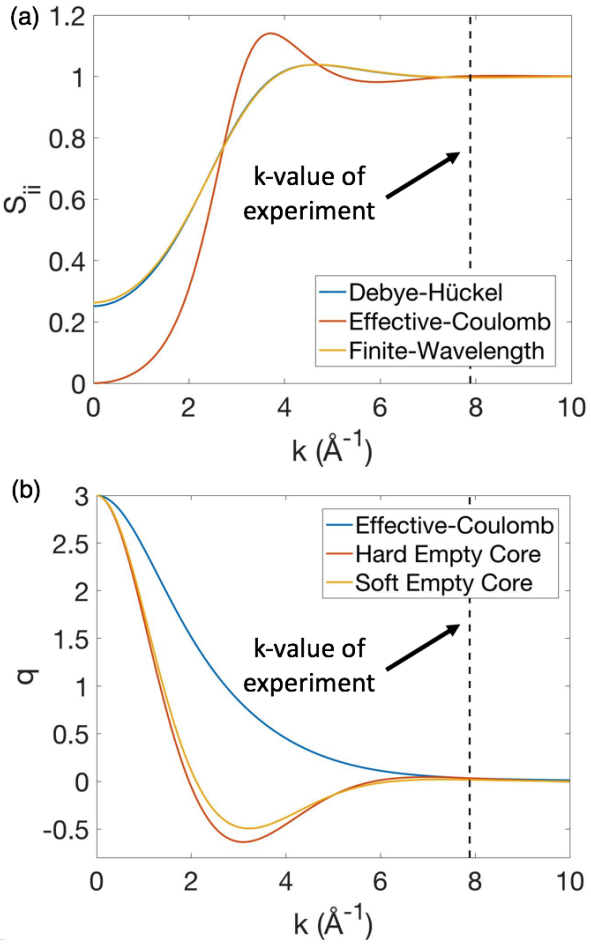

FIG. 4. a) The boron ion structure factor versus k for solid density (2.36 g cm^{-3}), 10 eV boron with $Z_B = 3.0$, as calculated by several models available in the MCSS code [40, 41]: Debye-Hückel [42], Effective-Coulomb, and finite-wavelength screening [34]. b) A plot of the B screening cloud contribution versus k as calculated by several models available for the electron-ion potential in the MCSS code [40, 41]: Effective-Coulomb, the Hard Empty Core, and the Soft Empty Core. In both cases, the experimental k-value of the experiment (7.9 Å^{-1}) is noted by the dashed vertical line. The ion structure factor converges to 1 and the screening cloud converges to 0 at the experimental k-value for all models considered. This increases confidence in the modeling of elastic scattering for this scattering geometry.

The literature contains many examples in which the inelastic scattering feature is compared with theoretically generated fits to infer plasma properties such as electron density and temperature [4, 23, 24, 26]. While the modeling behind the free-free scattering feature is thought to be well understood, the shape and scaling of the bound-free term can differ with different theoretical treatments [39, 43–47]. The bound-free term is of-

ten modeled using the impulse approximation, which is known to be a reasonable approximation for the case of $k \to \infty$ [28]. However, there remains uncertainty as to the proper scaling of the bound-free feature with respect to other features in the spectrum [43–45]. Because of such uncertainties, some recent work seeks to interpret scattering spectra outside of the Chihara decomposition, with methods like density functional theory [9, 35, 48]. For the case of these data, different methods of scaling the bound-free feature had little impact on the inferred temperature and is contained in the error bars.

More recent work in XRTS focuses on the information found in the elastic scattering feature; various authors use the strength of the elastic scattering feature to deduce plasma properties, such as the ion structure factor [32], the ionization state [4, 5, 30, 36, 49, 50], or the screening properties [34]. The values of $f(k)$, $q(k)$, and $S_{ii}(k,\omega)$ all depend on the magnitude of the scattering vector, k, which depends on the frequency of incident radiation, ω_i, and the scattering angle, θ. The ionic form factor, $f(k)$, is calculated by the Fourier transform of bound electrons around an ion species. The contribution from the electron screening cloud, $q(k)$, arises from the response of the free electrons to the ions, and is found to be best modeled by a finite wavelength screening method [5, 34]. The $S_{ii}(k)$ can be modeled with several different potentials, including Debye-Hückel [42], Coulomb, and finite wavelength. However, the Debye-Hückel potential is known to provide the best approximation in the case of partially ionized, moderate density, and low-Z plasmas [34].

Because $f(k)$, $q(k)$, and S_{ii} all contribute to elastic scattering signal strength, inferring properties like ionization from elastic scattering relies on accurate modeling of these features. It is possible to take measurements at high k-values in which $q(k)$ and S_{ii} approach their limiting values of 0 and 1, respectively. In that case, the values of S_{ii} and q become insensitive to model choice, which increases certainty in the measurement of $f(k)$ and thus the measurement of the ionization state. Figure 4 shows both q and S_{ii} as calculated by different models for the screening cloud and the static structure factor for solid-density boron at 10 eV. It is worth noting that the results here are effectively temperature independent within the WDM regime. The dashed vertical line marks the k-value of the experiment, 7.9 Å^{-1}. Figure 4 shows that the values of S_{ii} and q are model independent given the experimental geometry and energy of the probe source. By taking scattering measurements at such high k-values, we can be confident of the modeling of the elastic scattering and provide measurements of quantities that depend on the elastic scattering signal strength, like ionization states, with higher certainty.

V. DATA ANALYSIS AND DISCUSSION

We collected time-resolved XRTS measurements from boron cylinders and one measurement from a beryllium cylinder. In order to measure the plasma conditions, we compare the XRTS data to theoretically generated fits, using a χ^2 fitting method. Because the mass density is known *a priori*, only the electron temperature and ionization states remain to be identified by fitting synthetic scattering spectra to the measured data.

The raw data was processed to extract the spectra used in fitting. We subtracted a background to account for the emission from the still-warm x-ray converter foil; different background subtraction procedures were tested and found not to impact the temperature or ionization measurements. Figure 5 shows one of the spectra measured from boron, at (1.76 ± 0.20) ns. The right side of Figure 5 shows the spectrum along with several theoretically-generated spectra that vary with electron temperature (top right) and boron ionization (bottom right). All fits assume a solid mass density of 2.36 g cm^{-3}. The best fit is obtained with a temperature of $T_e = 8.2^{+2.3}_{-2.2}$ eV. The measurement also suggests that $Z_B < 3.1$; however, ionization states below $Z_B = 3.0$ are considered unphysical, as the boron L-shell is low enough in binding energy such that no L-shell electrons can remain in bound states at solid mass density. The left side of Figure 5 shows the chi-square map versus Z_B and T_e to illustrate the sensitivity of the fits to fitting parameters, with the 1σ confidence contour denoted by the dashed white curve.

Because boron is not expected to ionize into its K-shell until it reaches temperatures above 30 eV and the data suggest ionization states of $Z_B < 3.1$, we set $Z_B = 3.0$ and fit all spectra for electron temperature to measure temperature as a function of time. Figure 6 shows the measured temperatures and associated fitting uncertainties, along with several simulated temperature-versus-time curves, each generated with different incident laser intensities. As Figure 6 shows, the incident laser intensity affects the maximum temperature reached in the sample but does not affect the qualitative heating behavior; the temperature at the center of the cylinder increases rapidly while the laser drive is on and remains steady after the laser turns off, until the shock wave eventually reaches the center. The measured temperatures from the spectra are similar in value, which supports the heating trend observed in the simulations; namely, that the temperatures in the cylinder remain relatively constant after the laser drive turns off.

These measurements also demonstrate the power of this platform to measure electron temperature and ionization in order to benchmark models that predict the outcomes of radiative heating. Figure 6 shows simulated temperature versus time curves for laser intensities that range from $0.04I_0 = 40$ TW cm^{-2} to the nominal intensity, $I_0 = 1070$ TW cm^{-2}. As Figure 6 shows, simulations that use the nominal laser intensity over-predict the temperature reached in the cylinder by more than a factor of two and the best match with the data occurs when the laser intensity is decreased to $0.31I_0 = 330$ TW cm^{-2}. This could arise from modeling uncertainties in several

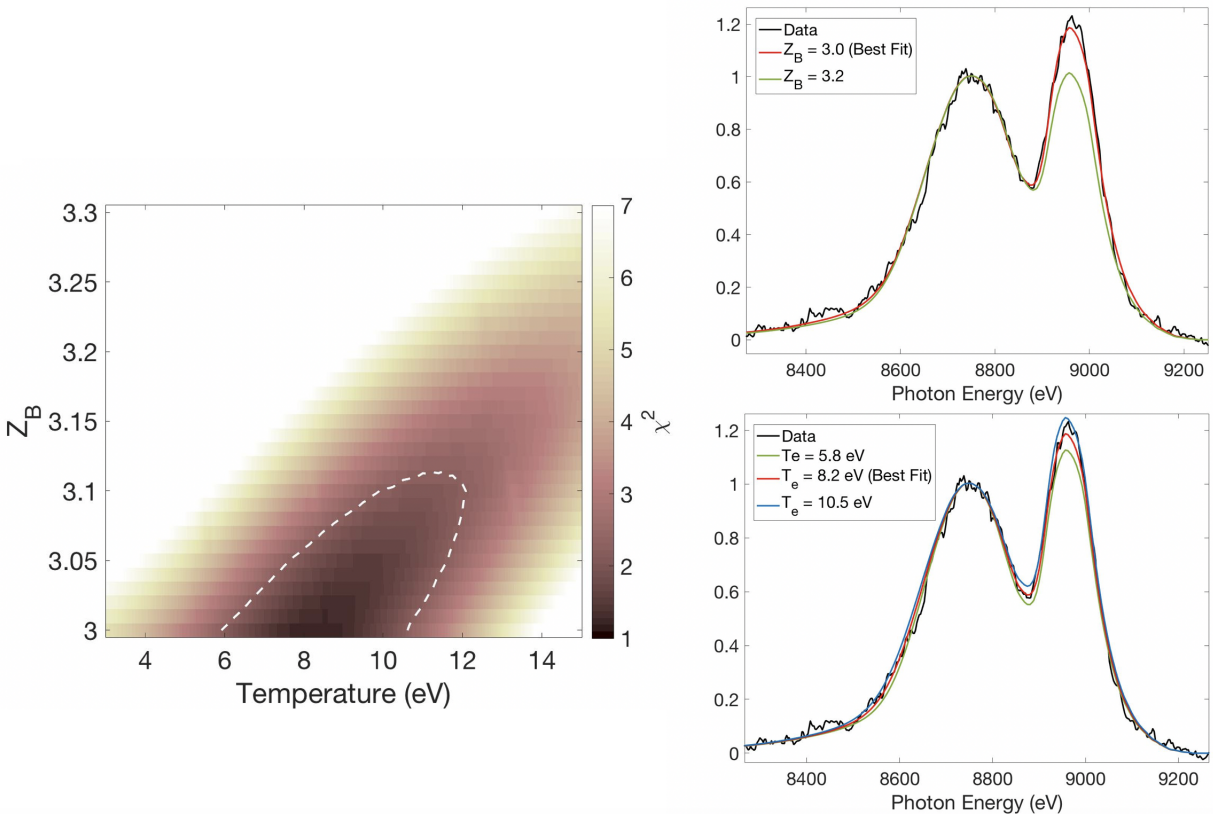

FIG. 5. Left: a χ^2 map versus electron temperature and B ionization state. 1σ confidence intervals are marked by the white dashed curve. The best fit is found at a temperature of $T_e = 8.6^{+2.7}_{-3.1}$ eV with $Z_B < 3.1$. Right: an illustration of ionization sensitivity (top right) and temperature sensitivity (bottom right) in the fitting. Both plots show the data and the best fit, as well as one or two other modeled spectra that vary ionization and electron temperature, respectively.

physical processes that govern radiative heating, including the conversion efficiency of laser to x-ray energy, uncertainty in the heater-foil thickness that could result in more self-attenuation of the x-rays, 2-D effects of heating that result in colder regions near the ends of the cylinders, uniformity of the laser drive on the cylinder, and the emission spectrum of the converter foil.

The plot of temperature sensitivity in the bottom right of Figure 5 demonstrates that increasing the temperature of a fit broadens the inelastic scattering peak, but has the primary effect of increasing the height of the elastic scattering peak relative to the inelastic peak (the spectra shown here are normalized to the heights of the inelastic peaks, for illustrative purposes). However, this effect is deceptive, as a change in temperature alone does not change the number of photons that scatter elastically for this scattering geometry. Rather, an increase in temperature broadens the free-free feature of the inelastic component of the spectrum which then adds with the elastic scattering feature to give an appearance of increased elastic scattering. Figure 7 shows the best fit to a boron spectrum to demonstrate how the free-free, bound-free, and elastic scattering features sum together to generate a full scattering spectrum. The high energy side of the free-free feature overlaps with the elastic scattering feature, so as the temperature increases and the free-free feature broadens, the unchanged elastic scattering feature and the broadened high energy side of the free-free feature add together to give a taller elastic peak. This results in a trade-off of fitting the spectrum both for temperature and ionization. However, as the χ^2 plot shows, the ionization and temperature can still be bound by fitting the complete spectrum.

We also measured and analyzed one spectrum from a beryllium cylinder that was isochorically heated by a silver x-ray converter foil. Figure 8 shows the best fit to the scattering spectrum, along with a χ^2 map versus ionization state and electron temperature. For the case of beryllium, the best fit was found to be $T_e = 6 \pm 5$ eV and $Z_{Be} < 2.2$. Here, ionization states below $Z_B = 2.0$ are considered unphysical. The large error bars from this measurement resulted from a high energy x-ray background generated by the Au shielding cone, as well as a lower signal-to-noise ratio due to fewer beams being used to generate the Zn x-ray source. The results of the Be measurements prompted a redesign of the shielding cone, as discussed in Section II, which significantly improved the resolution of the measurements. Future measurements on Be will take advantage of the optimized target design.

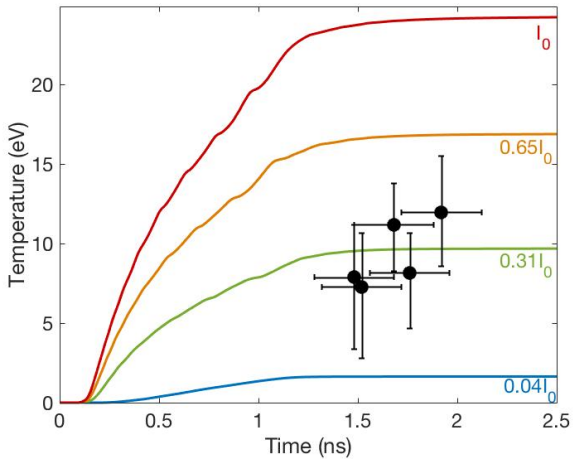

FIG. 6. A comparison of the experimentally measured electron temperatures versus time with predictions from 1-D radhydro simulations for several different incident laser intensities. The nominal laser intensity, indicated by I_0, was 1070 TW cm^{-2}. The power of the laser drive in the simulations had to be tuned to $0.31I_0$ match the measured temperatures, highlighting the importance of measuring the plasma conditions in radiative heating experiments.

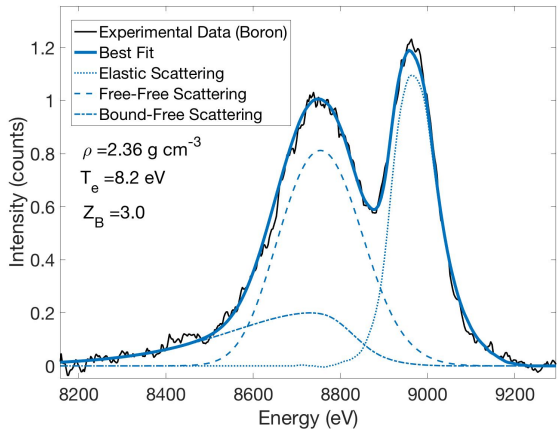

FIG. 7. The best fit to the B data at 1.68 ns, along with the individual contributions to the scattering spectrum. The blue wing of the free-free feature overlaps with the elastic scattering feature. Increased electron temperature broadens the free-free feature, which then adds with the elastic scattering feature to give the appearance of increased elastic scattering in the final spectrum.

Measurements like the ones presented in this paper will also benchmark simulations of XRTS spectra from materials at more extreme conditions. Recent literature contains conflicting predictions about the ionic form factor, f_k, in beryllium at high energy densities [51, 52], which has implications on the strength of elastic scattering and on the inference of ionization states. Density-functional-theory molecular-dynamics (DFT-MD) simulations for isochorically-heated Be presented in Fig. 3 in Ref. [51] predict that f_k is reduced by almost a factor of 2 compared to the simpler Hartree-Fock calculations. Similar simulations in Ref. [52] (shown in the top panel of Fig 3. in Ref. [52]) show that f_k is more consistent with Hartree-Fock. The data in this paper arise from comparatively well-known conditions, as the mass density is well-characterized and limited K-shell ionization is predicted to occur. Our Be data shown in Figure 8 have a ratio of elastic-to-inelastic scattering of 0.37 $\pm$ 0.04, and are thus consistent with predictions from Ref. [3] and Hartree-Fock calculations. The boron data show elastic to inelastic scattering ratios of 0.54 $\pm$ 0.05. Only at much higher densities of 10-times or more compression do we expect to see a reduction in the ionic form factor. Such conditions can and will be generated in capsule implosion experiments at the National Ignition Facility [53, 54], where the development of an experimental platform for XRTS measurements that uses the same scattering geometry (same scattering angle and photon energy) as the measurements reported in this paper is in progress [55].

VI. CONCLUSION

In this paper, we presented measurements of electron temperature and ionization from radiatively heated warm dense matter. The data were taken from a platform on the OMEGA laser that uses laser-driven x-ray converter foils to heat solid-density cylindrical samples. We performed a full analysis of spectra from solid-density B and Be samples and fit the spectra to obtain electron temperature and ionization. We also made time-resolved measurements of the temperature of the boron samples and compared the results to radiation hydrodynamics simulations. We found that the simulations over-predict the temperatures reached in the centers of the cylinders.

This platform can be extended to understand better the mechanism of radiative heating, as well as the properties of warm dense matter. Systematic studies could be performed to determine how parameters such as x-ray converter foil thickness, x-ray converter foil material, laser drive-time, and laser intensity affect the temperatures reached in the sample. In addition, temperatures in the sample could be increased in order to measure properties such as the onset of K-shell ionization in warm dense matter. The radius of the cylinder could be decreased to increase the sample temperature, or more beams used to heat the x-ray converter foil. Future experiments will further improve the error bars on the returned plasma parameters by increasing the signal-to-noise ratio of the measurement, presumably by adding more lasers to heat the x-ray backlighter or by summing repeated measurements. In addition, measurements at higher temperatures will be more accurate as the width of the inelastic Compton feature becomes more sensitive to electron temperature when the temperature exceeds the Fermi tem-

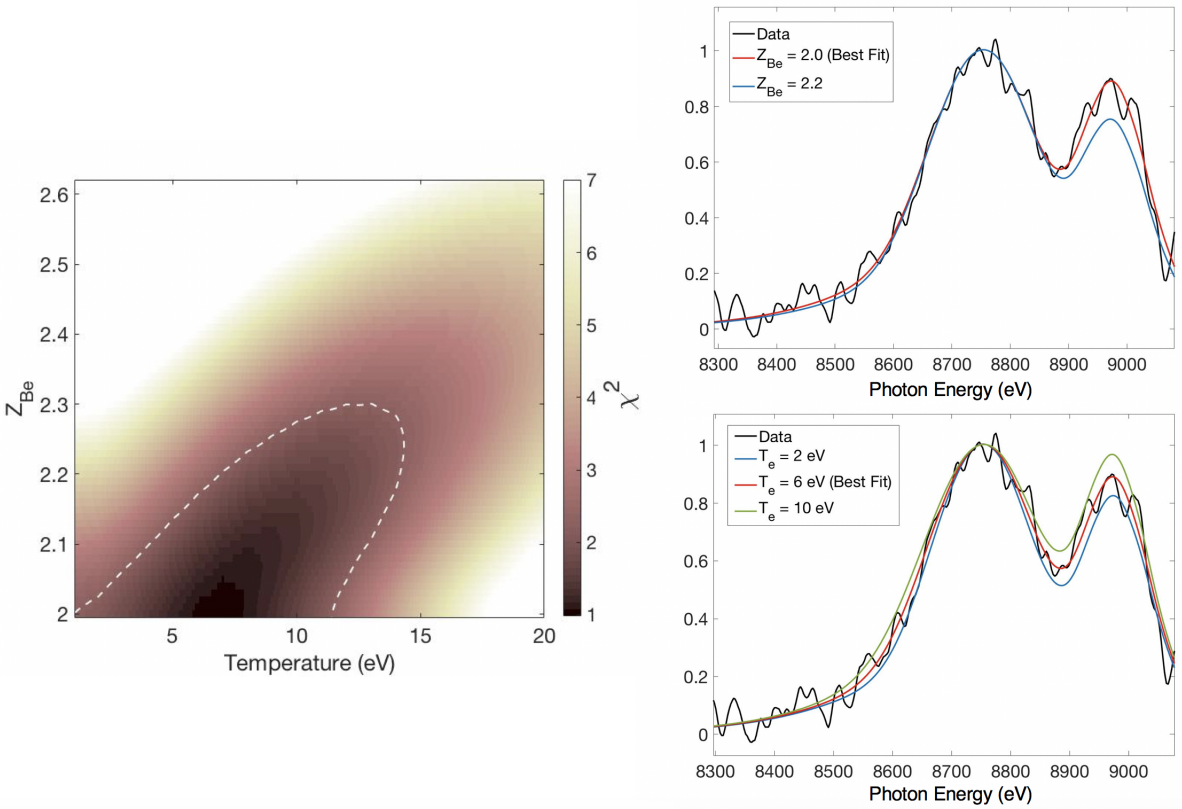

FIG. 8. Left: a χ^2 map versus electron temperature and Be ionization state. 1σ confidence intervals are marked by the white dashed curve. The best fit is found at a temperature of $T_e = 6^{+5}_{-5}$ eV with $Z_{Be} < 2.2$. Right: an illustration of ionization sensitivity (top right) and temperature sensitivity (bottom right) in the fitting. Both plots show the data and the best fit, as well as one or two other modeled spectra that vary ionization and electron temperature, respectively.

perature.

As it stands, the measurements presented in this paper highlight the necessity of using an experimental technique like XRTS to characterize the plasma conditions in radiatively heated warm dense matter. Simulations performed with the nominal laser intensity incident on the x-ray converter foil over-predict the temperatures reached in the samples by more than a factor of two; the laser intensity has to be decreased by nearly 70% to reproduce the measured values. The conclusions of previous experiments that relied on simulations to predict the plasma conditions from radiative heating, such as presented in reference [20], might need to be reconsidered. Future experiments will benefit by implementing a technique like XRTS to measure plasma conditions directly.

ACKNOWLEDGEMENTS

We thank the LLE and OMEGA laser staff for experimental support. We also thank Dirk Gericke and Dave Chapman for many discussions and contributions on the modeling of scattering spectra. This work was performed with the assistance of Lawrence Livermore National Laboratory (LLNL) under Contract No. DE-AC52-07NA27344 and supported by Laboratory Directed Research and Development (LDRD) Grant No. 18-ERD-033. MIT's was work was performed in part at the LLE National Laser Users Facility (Grant No. DE-NA0003539), and supported in part by US DOE (Grant No. DE-NA0002949) and LLE (subcontract Grant No. 416107-G). R.W.F. acknowledges support of this work by the U.S. Department of Energy, Office of Science, Office of Fusion Energy Sciences under Award Number DE-SC0018298, and the University of California Center for Frontiers in High Energy Density Science. This work was also performed with the support of the DOE NNSA Stewardship Science Graduate Fellowship program support Contract No. DE-NA0002135.

[1] B. Militzer, W. B. Hubbard, J. Vorberger, I. Tamblyn, and S. A. Bonev, The Astrophysical Journal Letters **688**, L45 (2008).

[2] J. R. Stauffer, G. Schultz, and J. D. Kirkpatrick, The Astrophysical Journal Letters **499**, L199 (1998).

[3] P. A. Sterne, L. X. Benedict, S. Hamel, A. A. Correa, J. L. Milovich, M. M. Marinak, P. M. Celliers, and D. E. Fratanduono, Journal of Physics: Conference Series **717**, 012082 (2016).

[4] L. B. Fletcher, A. L. Kritcher, A. E. Pak, T. Ma, T. Döppner, C. Fortmann, L. Divol, O. S. Jones, O. L. Landen, J. Vorberger, D. Chapman, D. O. Gericke, B. Mattern, G. T. Seidler, G. Gregori, R. W. Falcone, and S. H. Glenzer, Phys. Rev. Lett. **112**, 145004 (2014).

[5] L. B. Fletcher, H. J. Lee, T. Döppner, E. Galtier, B. Nagler, P. Heimann, C. Fortmann, S. L. Pape, T. Ma, M. Millot, A. Pak, D. Turnbull, D. A. Chapman, D. O. Gericke, J. Vorberger, T. White, G. Gregori, M. Wei, B. Barbrel, R. W. Falcone, C.-C. Kao, H. Nuhn, J. Welch, U. Zastrau, P. Neumayer, J. B. Hastings, and S. H. Glenzer, Nat. Photonics **9**, 274 (2015).

[6] S. H. Glenzer, O. L. Landen, P. Neumayer, R. W. Lee, K. Widmann, S. W. Pollaine, R. J. Wallace, G. Gregori, A. Höll, T. Bornath, R. Thiele, V. Schwarz, W.-D. Kraeft, and R. Redmer, Phys. Rev. Lett. **98**, 065002 (2007).

[7] C. A. Iglesias, High Ener. Dens. Phys. **7**, 38 (2011).

[8] D. Kraus, J. Vorberger, J. Helfrich, D. O. Gericke, B. L. Bachmann, V. Bagnoud, B. Barbrel, A. Blazevic, D. C. Carrol, W. Cayzac, T. Döppner, L. B. Fletcher, A. Frank, S. Frydrych, E. J. Gamboa, M. Gauthier, S. Göde, E. Granados, G. Gregori, N. J. Hartley, B. Kettle, H. J. Lee, B. Nagler, P. Neumayer, M. M. Notley, A. Ortner, A. Otten, A. Ravasio, D. Riley, F. Roth, G. Schaumann, D. Schumacher, W. Schumaker, K. Seigenthaler, C. Spindloe, F. Wagner, K. Wünsch, S. H. Glenzer, M. Roth, and R. W. Falcone, Phys. of Plasmas **21**, 056309 (2015).

[9] B. B. L. Witte, L. B. Fletcher, E. Galtier, E. Gamboa, H. J. Lee, U. Zastrau, R. Redmer, S. H. Glenzer, and P. Sperling, Phys. Rev. Lett. **118**, 225001 (2017).

[10] S. Zhang, B. Militzer, L. X. Benedict, F. Soubiran, P. A. Sterne, and K. P. Driver, The Journal of Chemical Physics **148**, 102318 (2018).

[11] O. Ciricosta, S. M. Vinko, H.-K. Chung, B.-I. Cho, C. R. D. Brown, T. Burian, J. Chalupský, K. Engelhorn, R. W. Falcone, C. Graves, V. Hájková, A. Higginbotham, L. Juha, J. Krzywinski, H. J. Lee, M. Messerschmidt, C. D. Murphy, Y. Ping, D. S. Rackstraw, A. Scherz, W. Schlotter, S. Toleikis, J. J. Turner, L. Vysin, T. Wang, B. Wu, U. Zastrau, D. Zhu, R. W. Lee, P. Heimann, B. Nagler, and J. S. Wark, Phys. Rev. Lett. **109**, 065002 (2012).

[12] R. W. Lee, S. J. Moon, H.-K. Chung, W. Rozmus, H. A. Baldis, G. Gregori, R. C. Cauble, O. L. Landen, J. S. Wark, A. Ng, S. J. Rose, C. Lewis, D. Riley, J.-C. Gauthier, and P. Audebert, J. Opt. Soc. Am. B **20**, 770 (2003).

[13] R. E. Marshak, The Physics of Fluids **1**, 24 (1958).

[14] R. E. Olson, R. J. Leeper, A. Nobile, J. A. Oertel, G. A. Chandler, K. Cochrane, S. C. Dropinski, S. Evans, S. W. Haan, J. L. Kaae, J. P. Knauer, K. Lash, L. P. Mix, A. Nikroo, G. A. Rochau, G. Rivera, C. Russell, D. Schroen, R. J. Sebring, D. L. Tanner, R. E. Turner, and R. J. Wallace, Physics of Plasmas **11**, 2778 (2004).

[15] C. A. Back, J. D. Bauer, O. L. Landen, R. E. Turner, B. F. Lasinski, J. H. Hammer, M. D. Rosen, L. J. Suter, and W. Hsing, Phys. Rev. Lett. **84**, 274 (2000).

[16] M. D. Rosen, Physics of Plasmas **6**, 1690 (1999).

[17] H. Lammer, F. Selsis, I. Ribas, E. F. Guinan, S. J. Bauer, and W. W. Weiss, The Astrophysical Journal Letters **598**, L121 (2003).

[18] J. R. Pritchard and S. R. Furlanetto, Monthly Notices of the Royal Astronomical Society **376**, 1680 (2007).

[19] A. Harpaz and S. Rappaport, Astrophys. J. **383**, 739 (1991).

[20] A. B. Zylstra, J. A. Frenje, P. E. Grabowski, C. K. Li, G. W. Collins, P. Fitzsimmons, S. H. Glenzer, F. Graziani, S. B. Hansen, S. X. Hu, M. G. Johnson, P. Keiter, H. Reynolds, J. R. Rygg, F. H. Séguin, and R. D. Petrasso, Phys. Rev. Lett. **114**, 215002 (2015).

[21] T. Boehly, R. McCrory, C. Verdon, W. Seka, S. Loucks, A. Babushkin, R. Bahr, R. Boni, D. Bradley, R. Craxton, J. Delettrez, W. Donaldson, R. Epstein, D. Harding, P. Jaanimagi, S. Jacobs, K. Kearney, R. Keck, J. Kelly, T. Kessler, R. Kremens, J. Knauer, D. Lonobile, L. Lund, F. Marshall, P. McKenty, D. Meyerhofer, S. Morse, A. Okishev, S. Papernov, G. Pien, T. Safford, J. Schnittman, R. Short, M. S. III, M. Skeldon, S. Skupsky, A. Schmid, V. Smalyuk, D. Smith, J. Soures, M. Wittman, and B. Yaakobi, Fusion Engineering and Design **44**, 35 (1999).

[22] F. Graziani, V. S. Batista, L. X. Benedict, J. Castor, H. Chen, S. N. Chen, C. A. Fichtl, J. N. Glosli, P. E. Grabowski, A. T. Graf, S. P. Hau-Riege, A. U. Hazi, S. A. Khairallah, L. Krauss, A. B. Langdon, R. A. London, A. Markmann, M. S. Murillo, D. F. Richards, H. A. Scott, R. Shepherd, L. G. Stanton, F. H. Streitz, M. P. Surh, J. C. Weisheit, and H. D. Whitley, High Ener. Dens. Phys. **8**, 105 (2012).

[23] S. H. Glenzer, G. Gregori, R. W. Lee, F. J. Rogers, S. W. Pollaine, and O. L. Landen, Phys. Rev. Lett. **90**, 175002 (2003).

[24] A. Kritcher, T. Döppner, C. Fortmann, T. Ma, O. L. Landen, R. Wallace, and S. H. Glenzer, Phys. Rev. Lett. **107**, 015002 (2011).

[25] S. H. Glenzer, G. Gregori, F. J. Rogers, D. H. Froula, S. W. Pollaine, R. S. Wallace, and O. L. Landen, Phys. Plasmas **10**, 2433 (2003).

[26] H. J. Lee, P. Neumayer, J. Castor, T. Döppner, R. W. Falcone, C. Fortmann, B. A. Hammel, A. L. Kritcher, O. L. Landen, R. W. Lee, D. D. Meyerhofer, D. H. Munro, R. Redmer, S. P. Regan, S. Weber, and S. H. Glenzer, Phys. Rev. Lett. **102**, 115001 (2009).

[27] K. Falk, C. L. Fryer, E. J. Gamboa, C. W. Greeff, H. M. Johns, D. W. Schmidt, M. Šmíd, J. F. Benage, and D. S. Montgomery, Plasma Physics and Controlled Fusion **59**, 014050 (2017).

[28] S. H. Glenzer and R. Redmer, Rev. Mod. Phys. **81**, 1625 (2009).

[29] G. Gregori, S. H. Glenzer, K. B. Fournier, K. M. Campbell, E. L. Dewald, O. S. Jones, J. H. Hammer, S. B. Hansen, R. J. Wallace, and O. L. Landen, Phys. Rev. Lett. **101**, 045003 (2008).

[30] D. Kraus, D. A. Chapman, A. L. Kritcher, R. A. Baggott, B. Bachmann, G. W. Collins, S. H. Glenzer, J. A. Hawreliak, D. H. Kalantar, O. L. Landen, T. Ma, S. Le Pape, J. Nilsen, D. C. Swift, P. Neumayer, R. W. Falcone, D. O. Gericke, and T. Döppner, Phys. Rev. E **94**, 011202 (2016).

[31] D. A. Chapman, D. Kraus, A. L. Kritcher, B. Bachmann, G. W. Collins, R. W. Falcone, J. A. Gaffney, D. O. Gericke, S. H. Glenzer, T. M. Guymer, J. A. Hawreliak, O. L. Landen, S. Le Pape, T. Ma, P. Neumayer, J. Nilsen, A. Pak, R. Redmer, D. C. Swift, J. Vorberger, and T. Döppner, Physics of Plasmas **21**, 082709 (2014).

[32] T. Ma, L. B. Fletcher, A. Pak, D. Chapman, R. W. Falcone, C. Fortmann, E. Galtier, D. O. Gericke, G. Gregori, J. Hastings, O. L. Landen, S. L. Pape, H. J. Lee, B. Nagler, P. Neumayer, D. Turnbull, J. Vorberger, T. G. White, K. Wünsch, U. Zastrau, S. H. Glenzer, and T. Döppner, Phys. of Plasmas **21**, 056302 (2014).

[33] K. Wünsch, P. Hilse, M. Schlanges, and D. O. Gericke, Phys. Rev. E **77**, 056404 (2008).

[34] D. A. Chapman, J. Vorberger, L. B. Fletcher, R. A. Baggot, L. Divol, T. Döppner, R. W. Falcone, S. H. Glenzer, G. Gregori, T. M. Guymer, A. L. Kritcher, O. L. Landen, T. Ma, A. E. Pak, and D. O. Gericke, Nat. Commun. **6**, 6839 (2015).

[35] A. N. Souza, D. J. Perkins, C. E. Starrett, D. Saumon, and S. B. Hansen, Phys. Rev. E **89**, 023108 (2014).

[36] A. M. Saunders, D. A. Chapman, A. L. Kritcher, M. Schoff, C. Shuldberg, O. L. Landen, S. H. Glenzer, R. W. Falcone, D. O. Gericke, and T. Döppner, High Energy Density Physics **26**, 86 (2018).

[37] J. MacFarlane, I. Golovkin, and P. Woodruff, Journal of Quantitative Spectroscopy and Radiative Transfer **99**, 381 (2006).

[38] J. Chihara, J. Phys. F: Met. Phys. **17**, 295 (1987).

[39] G. Gregori, S. H. Glenzer, W. Rozmus, R. W. Lee, and O. L. Landen, Phys. Rev. E. **67**, 026412 (2003).

[40] D. A. Chapman, *User guide and theoretical basis for the Multi-Component Scattering Spectra (MCSS) Thomson scattering analysis code (O)*, AWE (2017).

[41] D. A. Chapman, *Probing the Dynamic Structure of Dense Matter Using X-Ray Scattering*, Ph.D. thesis, University of Warwick (2015).

[42] P. Debye and E. Hückel, Phys. Z **24**, 185 (1923).

[43] B. A. Mattern, G. T. Seidler, J. J. Kas, J. I. Pacold, and J. J. Rehr, Phys. Rev. B **85**, 115135 (2012).

[44] B. A. Mattern and G. T. Seidler, Physics of Plasmas **20**, 022706 (2013).

[45] J. Nilsen, W. R. Johnson, and K. Cheng, High Energy Density Physics **9**, 388 (2013).

[46] R. Pratt, L. LaJohn, T. Suric, B. Chatterjee, and S. Roy, Nuclear Instruments and Methods in Physics Research Section B: Beam Interactions with Materials and Atoms **261**, 175 (2007).

[47] T. Surić, P. M. Bergstrom, K. Pisk, and R. H. Pratt, Phys. Rev. Lett. **67**, 189 (1991).

[48] A. D. Baczewski, L. Shulenburger, M. P. Desjarlais, S. B. Hansen, and R. J. Magyar, Phys. Rev. Lett. **116**, 115004 (2016).

[49] D. Riley, N. C. Woolsey, D. McSherry, I. Weaver, A. Djaoui, and E. Nardi, Phys. Rev. Lett. **84**, 1704 (2000).

[50] D. Kraus, J. Vorberger, D. O. Gericke, V. Bagnoud, A. Blažević, W. Cayzac, A. Frank, G. Gregori, A. Ortner, A. Otten, F. Roth, G. Schaumann, D. Schumacher, K. Siegenthaler, F. Wagner, K. Wünsch, and M. Roth, Phys. Rev. Lett. **111**, 255501 (2013).

[51] K.-U. Plagemann, H. R. Rüter, T. Bornath, M. Shihab, M. P. Desjarlais, C. Fortmann, S. H. Glenzer, and R. Redmer, Phys. Rev. E. **92**, 013103 (2015).

[52] J. Vorberger and D. O. Gericke, Phys. Rev. E **91**, 033112 (2015).

[53] D. T. Bishel, B. Bachmann, A. Yi, D. Kraus, L. Divol, M. Bethkenhagen, R. W. Falcone, L. B. Fletcher, S. H. Glenzer, O. L. Landen, M. J. MacDonald, N. Masters, P. Neumayer, R. Redmer, A. M. Saunders, B. Witte, and T. Döppner, Review of Scientific Instruments , accepted (2018).

[54] E. I. Moses, R. N. Boyd, B. A. Remington, C. J. Keane, and R. Al-Ayat, Physics of Plasmas **16**, 041006 (2009).

[55] D. Kraus, T. Döppner, A. Kritcher, A. Yi, K. Boehm, B. Bachmann, L. Divol, L. B. Fletcher, S. H. Glenzer, O. Landen, N. Masters, A. M. Saunders, C. Weber, R. Falcone, and P. Neumayer, J. Phys.: Conf. Ser. **717**, 012067 (2016).